

Repacking-Driven Compaction in the Spirit Mountain Batholith, Southern Nevada

Darien Florez^{1,2}, Christian Huber², Olivier Bachmann³, Alicia Sigworth⁴, Lily Claiborne⁴, and Calvin Miller⁴

¹MIT

²Brown University

³ETH

⁴Vanderbilt University

April 12, 2024

1. INTRODUCTION

The processes that influence differentiation in magma chambers and the rate at which the associated melt-crystal phases separate have important ramifications for volcanic-plutonic connections among silicic igneous rocks. Related to volcanic-plutonic connections among silicic igneous rocks is the identification of cumulate signature in plutons. The subtlety of crystal accumulation signals in silicic igneous rocks has led to their interpretation as representing a true melt composition and being genetically separated from volcanic rocks (Coleman *et al.*, 2004, Glazner *et al.*, 2004). While the petrological signature of the cumulate nature of silicic magmas is subtle, it is discernible nonetheless (Bachmann *et al.*, 2007, Deering & Bachmann, 2010, Gelman *et al.*, 2014). Knowledge of how melt loss occurs at melt fractions relevant to silicic magma chambers and the associated textural and chemical indicators can facilitate identification of cumulates in plutons. Furthermore, the rate at which the associated melt-crystal phases separate have important ramifications for volcanic hazards. Here, we investigate the Spirit Mountain Batholith (SMB) for chemical and textural evidence of crystallization-differentiation and phase separation by repacking-driven compaction (grain reorganizations).

The paper is organized such that we first introduce the geologic setting of the region and of the SMB in particular and provide evidence from previous studies supporting melt loss in the deeper parts of the SMB. Then, results of geochemical analyses are provided, including acquisition of major, minor, and trace elements of bulk rock SMB samples and results from plagioclase composition analyses. Subsequently, textural analyses of selected SMB samples are presented. We identify a near linear unmixing trend in major, minor, and trace element geochemistry defined by samples within a ca. 3 km transect at the base of the exposed batholith and pooled leucogranites near the top of the batholith. The plagioclase compositions suggest that the samples crystallized from the same parental magma and that the magma was less mafic than their bulk rock compositions. We then introduce a trace element model that allows melt and crystal to be lost to estimate relative melt loss (cumulate) or crystal loss (silicic cap) in the SMB. The benefit of this model is that it doesn't assume a particular separation mechanism; however, it is limited in that it doesn't provide the range of crystallinities over which melt is lost and doesn't allow calculation of trapped melt fractions. To accomplish this, we use an unmixing model that treats the analyzed samples as combinations between two different endmembers: melt and crystal at a certain crystallinity. The trapped melt fraction profile is then compared to results from a model of mush compaction based on a crystal repacking rheology to provide order of magnitude timescale estimates for the growth of the silicic cap (melt accumulation layer).

2. GEOLOGIC SETTING

The Colorado River extensional corridor in southern Nevada, California, and Arizona, is a ca. 70 x 250 km region consisting of highly extended crust (Fig. 1) (Faulds *et al.*, 2001, Faulds *et al.*, 1995, Faulds *et al.*, 1990, Howard *et al.*, 1996, Howard & John, 1987, Howard *et al.*, 1994). The corridor experienced crustal thinning from ca. 16 to 11 Ma and a flare-up of magmatism from ca. 18 to 8 Ma (Faulds *et al.*, 1995, Howard *et al.*, 1996). Several Miocene age plutons of felsic composition are found in the region, as well as extensive ash-flow tuffs, volcanic breccias, and lava flows (Fig. 1). Crustal sections were exposed in the region by tilting of fault blocks and subsequent erosion, the largest of which include upper to mid-crustal portions of the magmatic plumbing systems associated with region (Bachl *et al.*, 2001, Walker Jr *et al.*, 2007). There are several intrusive units in the corridor, the largest of which is Spirit Mountain batholith (Fig. 1).

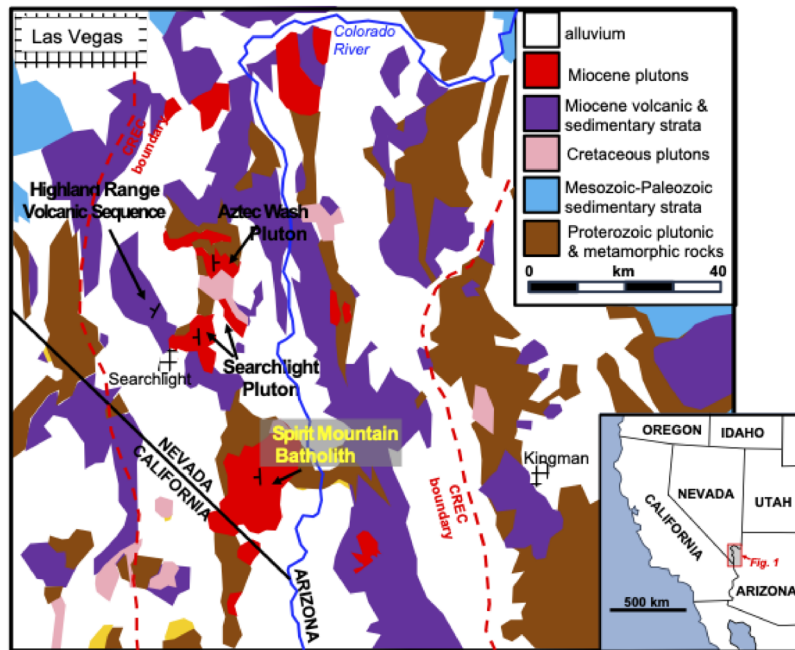


Figure 1: Regional geology of southern Nevada and parts of California and Arizona relevant to the Spirit Mountain batholith. Locations of the Spirit Mountain batholith and other Miocene plutons are highlighted.

Spirit Mountain batholith (SMB)

The SMB is a ca.10 x 20 km granitic pluton offering kilometers of largely uninterrupted exposure (Fig. 2). The pluton was emplaced in the northern Colorado River extensional corridor over a period of ~2 My (ca. 17.5–15.3 Ma) (Claiborne *et al.*, 2006, 2010, Walker Jr *et al.*, 2007). Post-emplacement tilting 45° W resulted in a cross-sectional window of the SMB exposed at the surface today (Faulds *et al.*, 1992, Haapala *et al.*, 2005, Howard *et al.*, 1994) (Fig. 2).

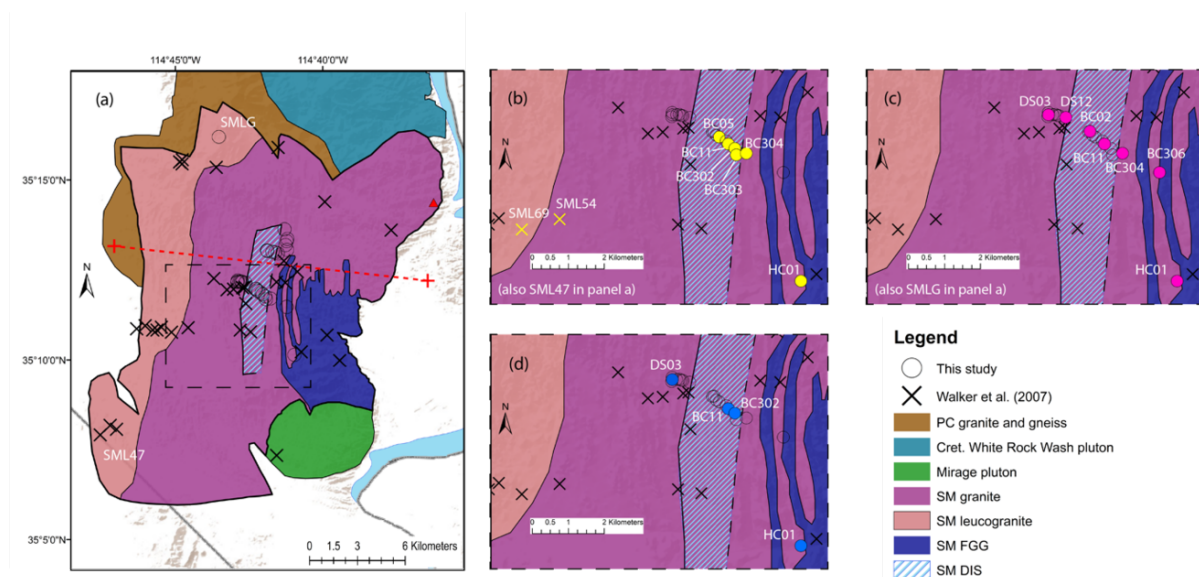


Figure 2: A) Spirit Mountain geologic map modified from Walker et. al (2007). Bulk rock geochemistry data is available for all samples in panel A. The pluton has been tilted ca. 45° westward during exhumation. In later sections, the distances above the deepest sample (red triangle in panel A) are calculated by projecting the samples orthogonally onto the dashed, red line in panel A. The distances are then adjusted for post-emplacement tilting of the batholith and are intended to reflect variations in paleo-depth. Panel B, C, and D show Spirit Mountain geology zoomed in. B) Samples highlighted in yellow are those included in transect analyzed using unmixing model developed in later sections. C) Samples highlighted in pink are samples analyzed via Electron Probe Microanalyzer (EPMA) in the present study. D) Samples highlighted in blue are those that are investigated texturally in later sections. In subsequent figures, samples from this study and Walker et. al (2007) are no longer distinguished, for readability, and samples included in transect appear yellow and all other samples are white.

The main units in the batholith, identified in Claiborne *et al.*(2006) and Walker Jr *et al.* (2007), include the Spirit Mountain granite (SMG), Spirit Mountain leucogranite (SMLG), the fine-grained granite (FGG) suite, diorite sheets, dike swarms, and the Mirage pluton. The SMG and SMLG were combined in Walker Jr *et al.* (2007) and referred to simply as “SMG”. The SMG and SMLG make up the vast majority of the pluton.

Walker Jr *et al.* (2007) documented a continuous range in wt % SiO_2 of ca. 61 – 79 between the SMG and SMLG (excluding the more mafic diorite sheets). Leucogranite samples are typically fine- to medium-grained and contain ca. 10% plagioclase, 40 – 50% alkali feldspar, 30 – 40 % quartz, and small amounts of biotite (Walker Jr *et al.* , 2007). The shallowest (western most) portions of the SMLG include aplite sheets, granite porphyry, and miarolitic cavities. SMG samples, on the otherhand, are coarse (millimeter scale) and contain 20 – 50 % to plagioclase, 30 – 50 % alkali feldspar, 5 – 30 % quartz, and 3 – 15% biotite. The deepest (eastern most) and most quartz-poor samples are enriched in major, minor, and trace elements consistent with accumulation of early crystallized phases (i.e., Sr, Ba, and Al_2O_3 suggesting accumulation of feldspars). This suggests mechanical phase separation may be important in the SMG; however, the extent and mechanism responsible for separation remain unconstrained.

The FGG, Mirage pluton, and dike swarms are similar in texture (uniformly fine-grained), composition

(71-74 wt % SiO_2), and in general relative timing (late stage), as they all intrude the SMG. The FGG and diorite units are found as sill-like sheets, pods, and pillows mostly towards the base of the exposed batholith, while the Mirage pluton intrudes the southern portion of the SMG. Several magmatic units with similar traits (composition, grain size, field relations) are found within other intrusive Miocene complexes in the region, suggesting that such magmas were perhaps the parental magmas from which different portions of the SMG differentiated (Gualda *et al.*, 2023). Here, we investigate the SMB (SMG in particular) for records of phase separation to explore the mechanisms that lead to chemical differentiation and the formation and accumulation of evolved melt caps.

3. ANALYTICAL METHODS

Geochemistry

Forty-two samples were collected in the field, of which thirty were analyzed for elemental compositions. Whole rock powders were prepared from fresh samples using an alumina ceramic shatter box and analyzed for major and trace elements at the Peter Hooper GeoAnalytical Lab at Washington State University. Major and minor elements were obtained using a Thermo-ARL automated X-ray fluorescence spectrometer (XRF). Trace elements were obtained using an Agilent inductively coupled plasma mass spectrometer (ICP-MS). The sample locations are shown in Fig. 2 and represented as circles in panel A. A full table summarizing the location and chemistry of the samples can be found in the supplementary Tables 1, 2, and 3. Example thin sections of samples are shown in Fig. 3.

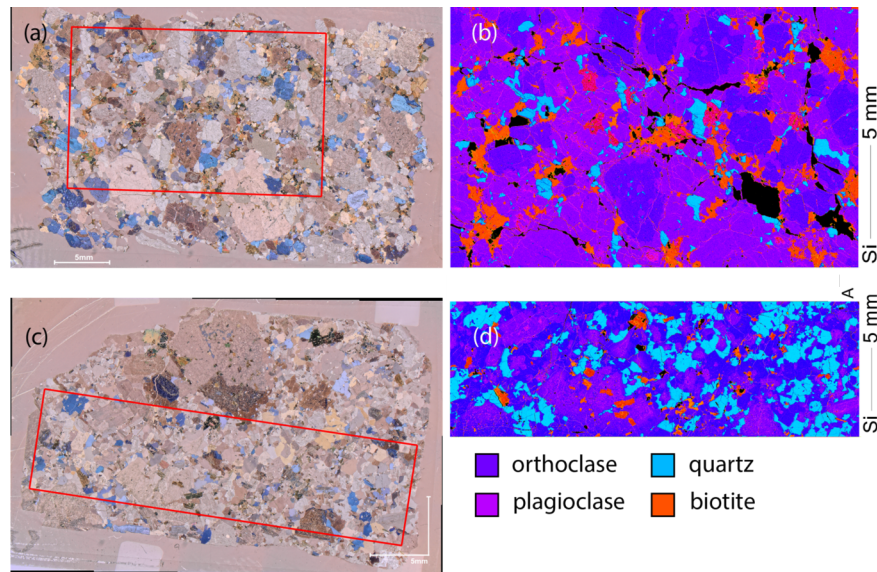


Figure 3: Thin sections of two SMB samples. A) XPL and B) WDS Si map scan of HC01 from Spirit Mountain granite (SMG) unit, near the bottom of the section. Panel C and D are the same, for scans of BC02 sample from Spirit Mountain granite unit from the middle of the section. The main phases are quartz, biotite, plagioclase, and alkali feldspar (turquoise, orange, purple, and blue phases in right column, respectively).

Plagioclase compositions and maps

Eight thin section samples were analyzed using five wavelength-dispersive X-ray spectrometers (WDS) to obtain precise, quantitative compositional maps. The sample locations are shown in Fig. 2 and are represented by pink circles. Thin sections were coated with an approximately 20 nm thick carbon layer. The maps were produced at the Department of Earth Sciences, ETH Zurich, using a JEOL JXA-8230 Electron

Probe Microanalyzer (EPMA) instrument. The applied acceleration voltage was 15 kV with a 100 nA beam current. A pixel size of 15 mm x 15 mm, a dwell time of 35 ms, and a probe diameter of 10 mm was used for samples BC306, BC304, BC11, BC02, DS12, and DS03. For samples HC01 and SMLG, a pixel size of 25 mm x 25 mm, a dwell time of 50 ms, and a probe diameter of 25 mm was used. The resulting scans allow for precise elemental maps of the sections analyzed and the calculation of chemical formulas of phases of interest. Here, we investigate plagioclase due to its prolonged duration on the liquidus and because the composition records changes in the melt with which it is in equilibrium.

Texture analysis

Four samples cut along planes striking NS and dipping 45° E (approximately paleovertical) were analyzed in thin section using a petrographic microscope at the Nature Lab at the Rhode Island School of Art and Design. The microscope renders mosaics of each sample consisting of stitched together portions of an individual sample. The orientation of the planes along which thin sections were made was chosen to investigate whether magmatic foliation due to gravity was detectable in samples. Grain boundaries were identified using image processing, following the technique implemented by Barraud (2006). This technique makes use of the watershed segmentation function of the Insight Toolkit (ITK). ITK is an open-source and cross-platform library that is implemented in C++. The watershed segmentation technique is applied to the images using the function *WatershedSegmentation1.cxx* included with the ITK examples build. The function uses an anisotropic diffusion filter to smooth the image and then converts the image to greyscale. A gradient function is then applied to the image which is then saturated to allow for the segmentation of individual grains. The grain boundary images are then thresholded and analyzed in ImageJ, approximating individual grains as ellipses, to obtain information about the orientation of each grain/ellipse.

4. ANALYTICAL RESULTS

Major, minor, and trace element geochemistry

The granitic samples obtained of the Spirit Mountain batholith record an almost continuous chemical gradation from 61 to 79 wt% SiO₂ (Fig. 4 and 5). The variation of any particular major element reaches a minimum at around 72 – 74 wt% SiO₂ and increases as wt% SiO₂ decreases. At SiO₂ contents greater than 72 – 74 wt%, the spread in oxide concentrations tends to either cluster or spread again (Fig. 4). Similar trends occur in minor and trace elements when plotted as a function of wt% SiO₂ (Fig. 4 and 5). The samples highlighted in yellow in Fig. 2b are plotted in yellow in Fig. 4 and 5 and define a near linear trend in major, minor, and trace element space.

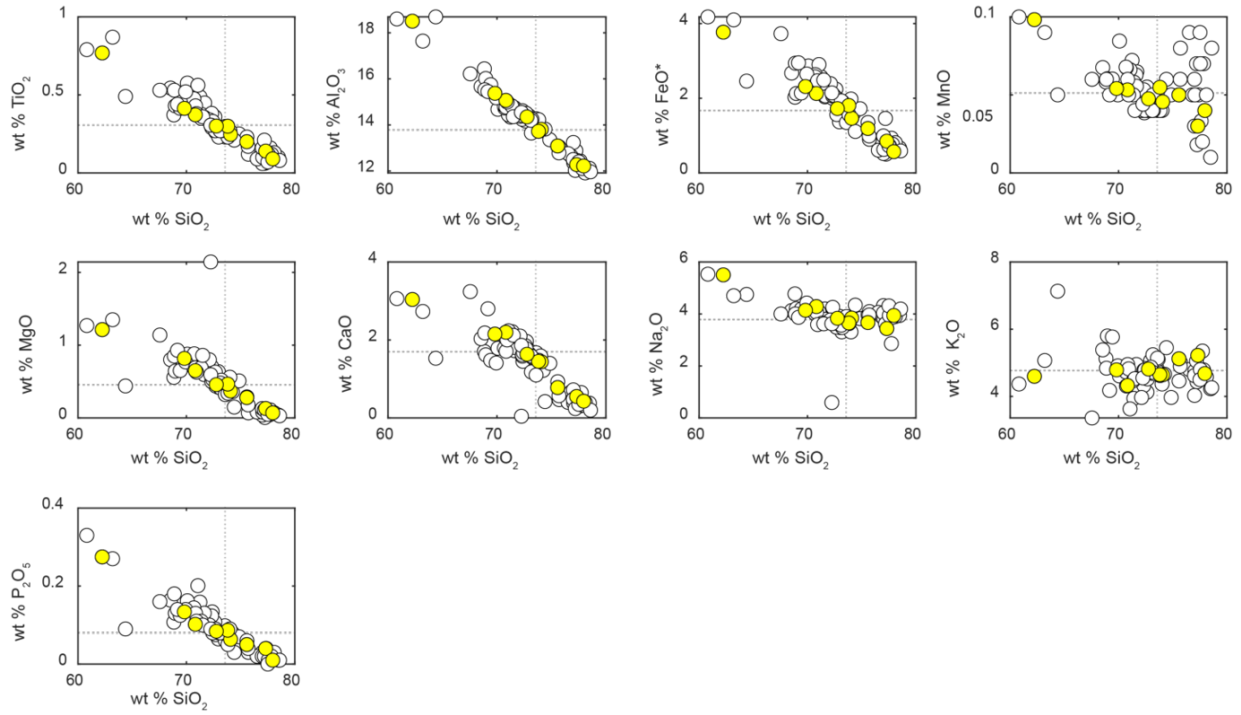


Figure 4: Harker diagrams for major element oxides for SMB samples of this study and of Walker et. al (2007). Total Fe expressed as FeO. Samples in yellow are analyzed in later sections using unmixing model. All other samples are shown in white. Grey lines indicate the assumed parental magma composition in later sections.

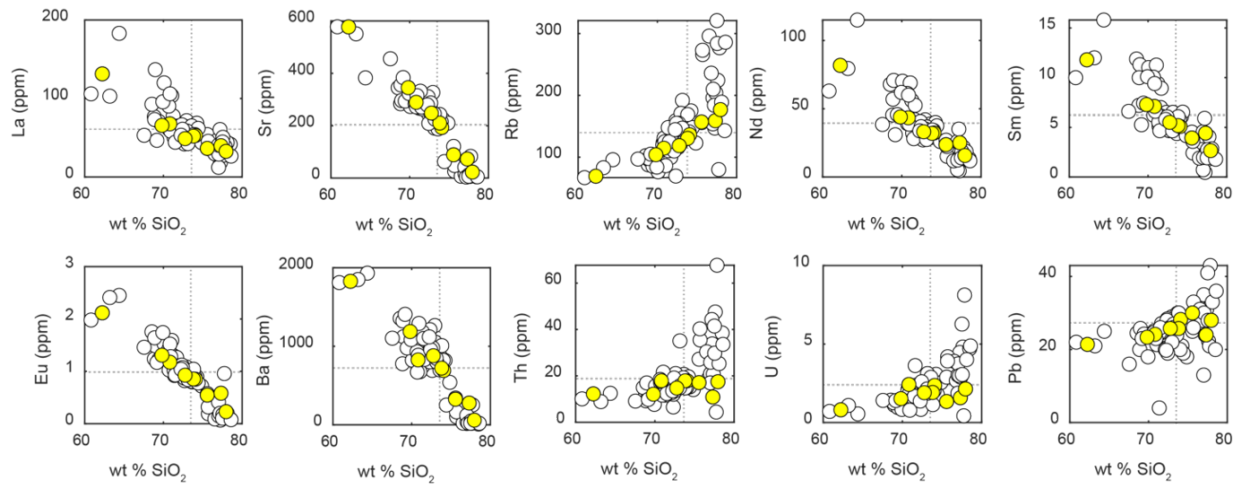


Figure 5: Selected trace elements plotted as a function of wt % SiO₂. Samples with low wt % SiO₂ are enriched in compatible trace elements such as Sr. Samples in yellow are analyzed in later sections using unmixing model. All other samples are shown in white. Grey lines indicate the assumed parental magma composition in later sections.

Plagioclase compositions

An example elemental plagioclase map is shown in Fig. 6a. The molar anorthite number (An#; mol CaO/[CaO + NaO_{0.5} + K_{0.5}]) is calculated for each plagioclase pixel of the scan and shown in the distributions of Fig. 6b. The statistical mode for distributions in six of the seven samples are relatively consistent (centered at around An # 0.15 – 0.25). This is especially surprising considering the range in bulk wt % SiO₂ (62 to 74 wt %) of these six samples (Fig. 6c). One sample, SMLG, however, has a distinctly lower modal An # (about 0.05) and a considerably higher wt% SiO₂ value (78 wt%). Finally, for comparison, the expected equilibrium range of molar anorthite numbers in plagioclase as a function of bulk rock molar anorthite number is shown in Fig. 6d. The range in equilibrium plagioclase compositions derives from the equilibrium constant, K_{eq}, from the exchange reaction between plagioclase and melt (Drake, 1976, Dungan *et al.*, 1978, Putirka, 2008, Rhodes *et al.*, 1979). Here, K_{eq} = 0.10 ± 0.05 (Putirka, 2008), and depends on the molar ratio of AlO_{1.5}/ SiO₂. The upper and lower bounds for the equilibrium range plotted in Fig. 6c are obtained by taking the lowest and highest AlO_{1.5}/ SiO₂ ratios amongst the yellow samples in Fig. 6c. The grey circles in Fig. 6c are calculated using the bulk molar anorthite number and AlO_{1.5}/ SiO₂ ratio for each sample to predict the equilibrium molar anorthite number in plagioclase. Fig. 6d highlights that the analyzed samples are shifted off the equilibrium line and have anorthite contents lower than would expect given that of the bulk rock. SMLG, however, approaches equilibrium.

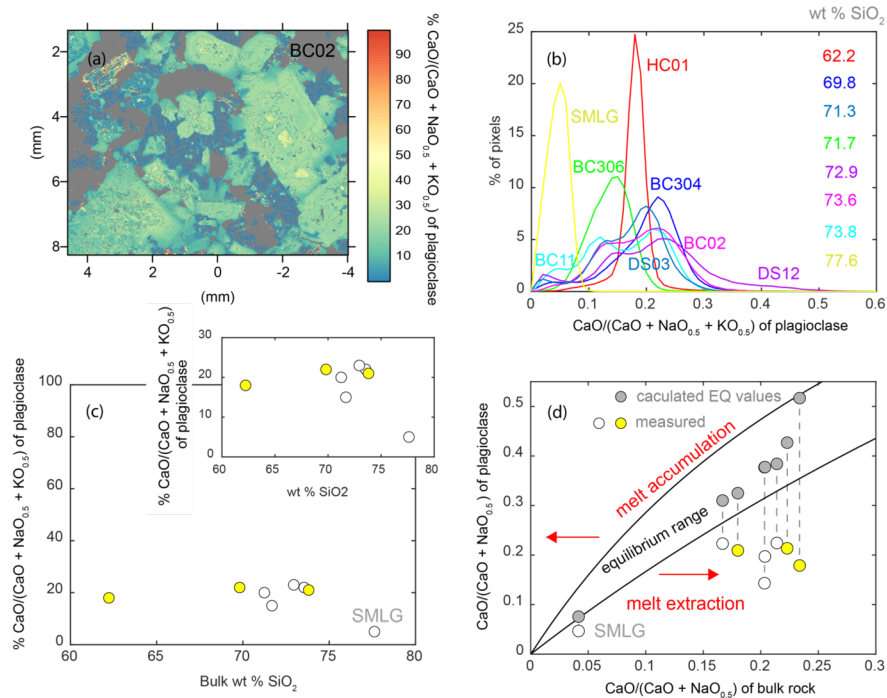


Figure 6: A) quantified elemental scan of sample BC02 showing molar CaO/[CaO + NaO_{0.5} + K_{0.5}] in plagioclase and alkali feldspar (values between ca. 0 – 55 %). Plagioclase is light blue, alkali feldspar is darker blue, and the grey areas are non-feldspar phases. B) Frequency distribution showing percent of pixels in plagioclase with a given An #. C) Statistical mode of each distribution plotted in panel B as a function of wt % SiO₂ of the bulk sample. D) Statistical mode of each curve plotted in panel B as a function of CaO/[CaO + NaO_{0.5} + K_{0.5}] in the bulk rock. For comparison, expected mineral (plagioclase) and liquid equilibrium values are superimposed using K_{eq}(An-Ab)^{pl-liq} = 0.10. Grey circles are calculated using the bulk molar anorthite number and AlO_{1.5}/ SiO₂ ratio for each sample to predict the equilibrium molar anorthite number in plagioclase. Results suggest that SMG samples analyzed are out of equilibrium with their bulk rock and are more evolved than expected given their, in cases, more mafic bulk rock composition. Samples in yellow are analyzed in later sections using unmixing model. All other samples are shown in white.

Texture and fabric

The maps of identified grains and grain boundaries for DS03, BC11, BC302, and HC01 (shallowest to deepest in terms of paleodepth, least to most mafic, and highest to lowest Rb/Sr ratios) are shown in Fig. 7. The thin sections were cut along planes that were originally perpendicular to the surface (assuming a 45° westward postemplacement tilt) and were striking NS but that had since been tilted (Fig. 7a). Only grains away from the edges were analyzed leading to some vacant space on certain portions of the maps. Rose diagrams (last two column of Fig. 7) show the number of particles oriented at a given angle (azimuth) with respect to the bottom edge of the image. The tan rose diagrams include all identified grains while the pink rose diagrams only include phenocryst grains (euhedral plagioclase, alkali feldspar, and biotite) for each sample. The intensity of fabric development can be described by the alignment factor (Barraud, 2006). The alignment factor (AF) can be calculated by first introducing an orientation tensor, T^n , for each grain:

$$T^n = L_n \begin{bmatrix} \alpha_n & \text{amp}; \cos \alpha_n \sin \alpha_n \\ \cos \alpha_n \sin \alpha_n & \text{amp}; \alpha_n \end{bmatrix} \quad (1)$$

Here, n , refers to a grain of interest and L is the major axis length. The bulk orientation tensor, M_{ij} , can be related to T^n as:

$$2. \quad M_{ij} = \frac{1}{N} \sum_1^N T_{ij}^n \quad (2)$$

Finally, AF is defined as:

$$\text{alignment factor (AF)} = 100 \times \frac{e_1 - e_2}{e_1} \quad (3)$$

where e_1 and e_2 are eigenvalues of M_{ij} . Conceptually speaking, AF represents the extent of agreement between orientations of individual grains.

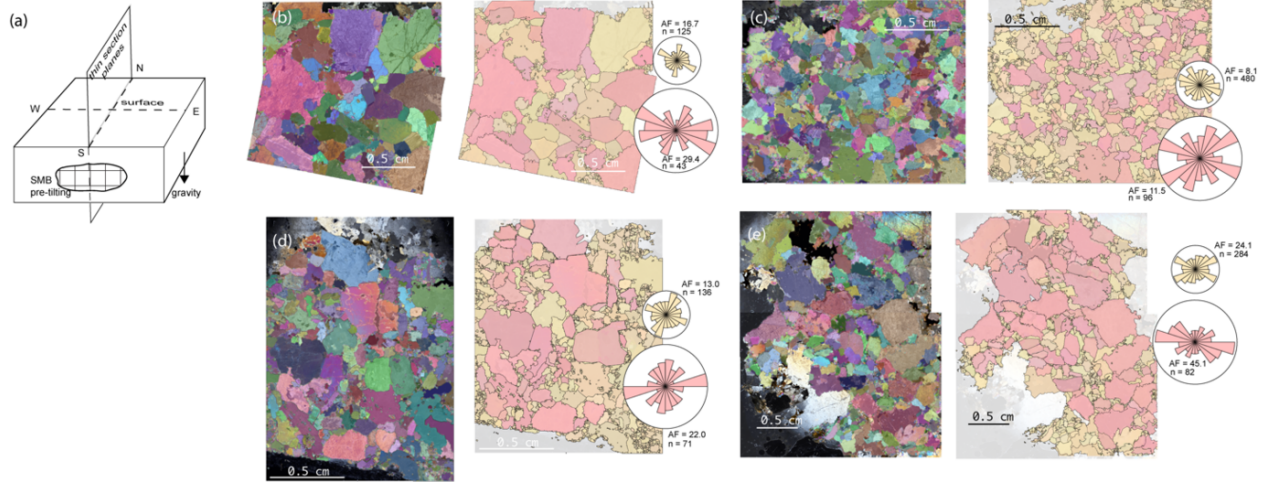


Figure 7: A) Orientation for textural analysis and analysis results for B) DS03, C) BC11, D) BC302, and E) HC01. A) Schematic showing the plane in which thin sections were prepared relative to original orientation (pre-tilting) of SMB. The left panel in B, C, D, and E includes identified grains and grain boundaries, the identification of which is described in the main text. Each color corresponds to an individual grain and has no relation to mineralogy. The right panel in B, C, D, and E includes identified grains and grain boundaries, but feldspar and biotite phenocrysts have been highlighted with a pink-ish hue and all other grains with tan-ish hue. The right panel in B, C, D, and E also includes rose diagrams which display the number of grains whose long axis is aligned at a given angle. The tan rose diagrams include all grains (no mineralogic distinction), while pink rose diagrams only take into account feldspar and biotite phenocrysts. The AF (alignment factor), which describes the extent of foliation, of each grain population is tabulated and displayed with the rose diagrams. The angles are measured with respect to the bottom edge of the image.

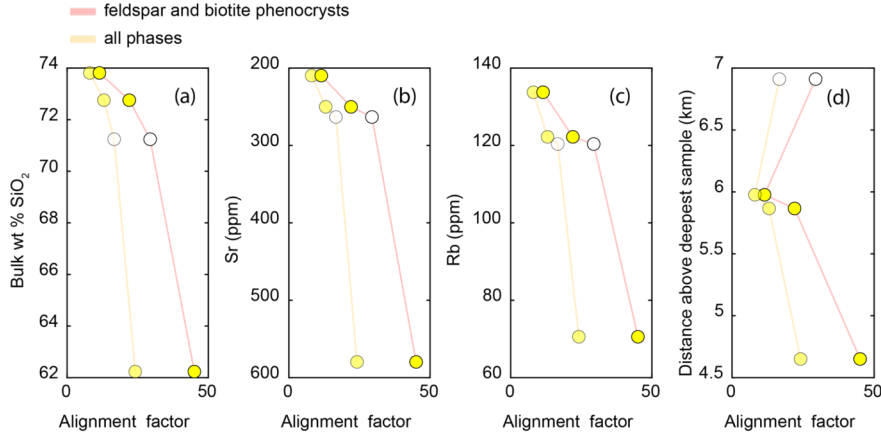


Figure 8: A) wt % SiO₂, B) Sr concentration, C) Rb concentration, and D) distance above deepest sample of pluton as a function of alignment factor (AF). An alignment factor (AF) of 100 corresponds to populations of particles with identical orientations, while an alignment factor of 0 corresponds to no preferred orientation. Here, the distance above deepest sample is calculated by projecting the samples orthogonally onto the dashed, red line in panel A of Fig. 1. The distances are relative to the orthogonal projection of the deepest sample, represented by a red triangle in panel A of Fig. 1. Data points here correspond to samples shown in Fig. 7. Faded data points are AF values that correspond to all grains and completely opaque data points are AF values calculated for only feldspar and biotite phenocrysts. Samples in yellow are analyzed in later sections using unmixing model. All other samples are shown in white.

Fig. 8 shows the AF for each sample that was analyzed texturally, for both all grains (faded markers) and phenocryst grains (solid markers). Fig. 7 and 8 illustrate that the intensity of SPO (both for all grains and phenocryst grains) observed in HC01 (the deepest sample) is the strongest, while SPO in BC302 (shallower) is weaker in intensity. BC11 (shallower than BC302), on the other hand, exhibits the weakest SPO. The shallowest sample, DS03, has the second most visible SPO. The SMG samples exhibit AFs that are inversely correlated with wt % SiO₂ and Rb and positively correlated to Sr (Fig. 8). The AF of yellow samples in Fig. 8 (analyzed in later sections using unmixing model) correlate inversely with distance above deepest sample. The phenocryst population was identified in cross polarized light on the basis of interference color, euhedrality, lack of undulose extinction, and twinning (feldspars), and alteration and spottiness. Rose diagrams and the AF for all grains are included for comparison to ensure that bias introduced by manually assigning mineralogies to the identified grains is minimized.

5. TRACE ELEMENT MODELING AND RHYOLIT-MELTS CALIBRATION

We implement a trace element (TE) model based on Gelman *et al.*(2014) in order to investigate if the range in trace elements recorded by the SMB is consistent with crystallization and variable melt loss from a single parental magma composition. The box model considers the evolution of the concentration of a given trace element during crystallization in three separate reservoirs: crystal, melt, and lost melt (in alternate simulations we consider crystal, melt, and lost crystals). The reason for this formulation is because accumulating feldspars (melt loss) can explain SMB samples enriched in Sr, while accumulating melt (crystal loss) can explain SMB samples depleted in Sr. In the model, crystal and melt reservoirs are coupled or grouped together and comprise the synthetic sample (Fig. 9). Lost melt, on the other hand, is removed from the sample (Fig. 9 and 10). Strictly speaking, however, the fundamental equations used to solve for the evolution of the trace elements of interest (Sr and Rb) assume fractional crystallization. This choice is governed by the diffusivity of the trace element of interest and the longevity of the magma system at elevated temperatures. Gelman *et al.* (2014) demonstrated that for Sr the results are relatively insensitive to this choice. In the box model, the sample is initially considered entirely molten and subsequently the mass of the

trace element is partitioned between crystals and melt as crystallization persists. Either reservoir (crystal or melt) can be incrementally lost; however, only lost melt or crystals are separated or “lost” from the sample (Fig. 9 and 10). If no mass is lost, all of the melt will convert to crystal and the final sample concentration (concentration of TE of interest in crystal reservoir once all melt has crystallized) will be equivalent to the starting concentration of the parental melt. However, if a portion of melt is lost, only the melt that remains is converted to the crystal reservoir that comprise the final sample (Fig. 10). Here, the final concentration of the sample relative to the initial concentration of the sample will change as total sample mass has decreased, while, depending on the compatibility of the TE of interest, the mass of the TE in the crystals potentially remains the same. Allowing crystal loss similarly decreases the sample mass; however, the effect on the final concentration of the sample will be the inverse of the case of melt loss (loss of melt for a compatible TE increases TE concentration in the final sample relative to initial whereas crystal loss decreases the final concentration).

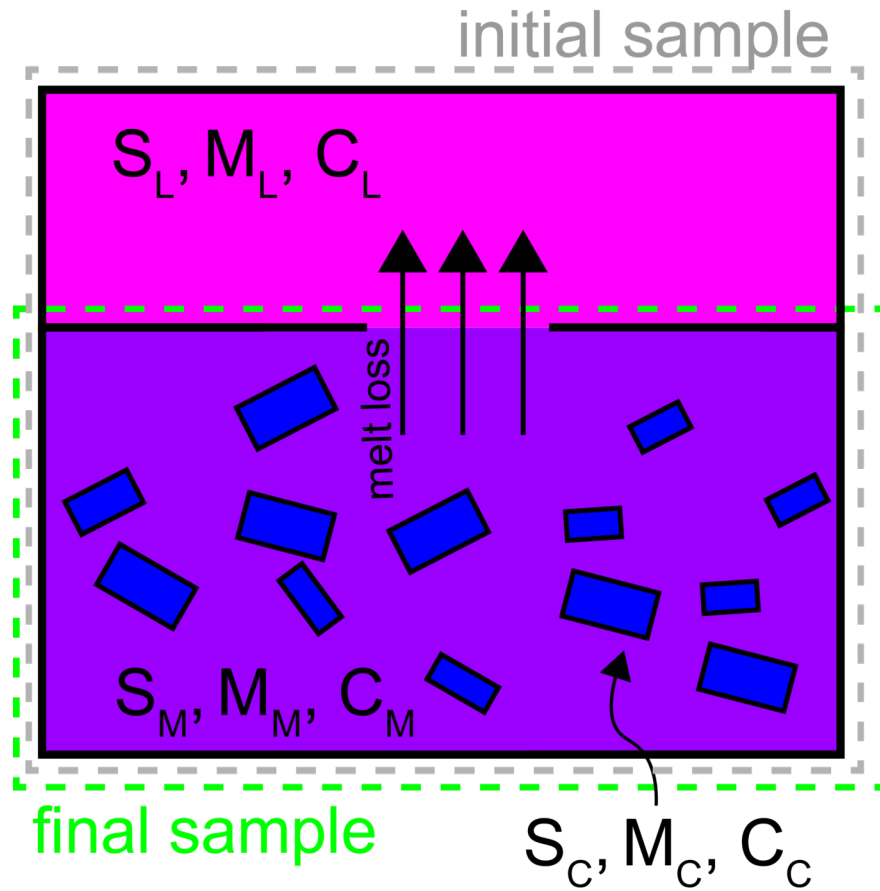


Figure 9: Schematic diagram of trace element box model developed in this study for the case of melt loss. Four reservoirs exist: mass of melt, M_M , mass of melt lost, M_L , mass of crystallized solid, M_C , and mass of crystal lost, M_{CL} . M_{CL} is not shown in the illustration but is similar to M_L except that it takes mass away from the solid. Simulations take into account either no mass loss or either (not both) melt or crystal loss. The sum of mass in all reservoirs is constant M_0 , the initial mass of melt. Each reservoir has an associated concentration of the trace element of interest which is solved for using eqs. 1-4. Here, S is mass of trace element of interest, M is mass of reservoir, and C is concentration of trace element. In the case of melt loss, the sample is comprised of only retained melt (melt reservoir) and accumulated crystals (crystal reservoir).

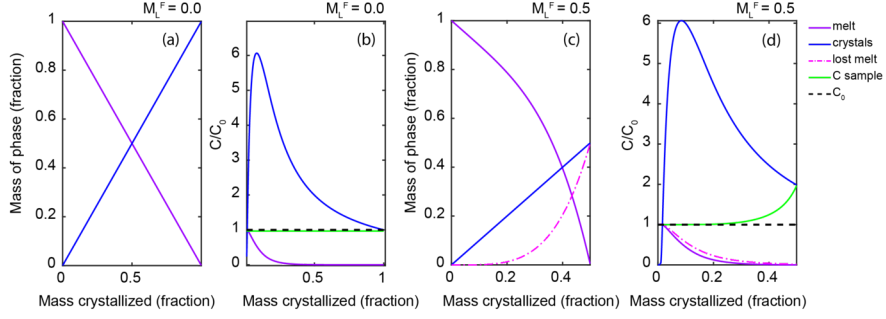


Figure 10: Example outputs of trace element model. A) Evolution of mass of each reservoir as a function of total mass crystallized. B) Evolution of concentration of Sr in each reservoir. In A) and B) the final mass fraction of melt loss, $M_L^F = 0.7$. C) and D) show the same as panel A and panel B, respectively, except with $M_L^F = 0.5$. Here, the bulk partition coefficient (included in later sections) is constrained using rhyolite-MELTS simulations.

Table 1. Symbols and definitions.

Symbol	Definition
C	concentration
M	mass of reservoir
D	bulk partition coefficient
K_D	partition coefficient
S	mass of trace element
C (subscript)	crystal reservoir
b (subscript)	bulk
M (subscript)	melt reservoir
L (subscript)	melt lost reservoir
C_{sample}	TE concentration in sample (crystals + melt in Figure 9)
M_L^F and M_{CL}^F	terminal amount of lost melt or lost crystal, respectively

To develop the model, we solve for the change in concentration of a trace element in the melt:

$$\frac{dC_M}{dM_C} = \frac{C_M}{M_M} (1 - D) \quad (4)$$

Here, C_M is the concentration of a particular trace element in the melt, M_C is the mass of crystallized solid, M_M is the mass of melt, and D is the bulk partition coefficient (see Table 1 for symbols and definitions). Eq. (1) describes the change in concentration dC_M in the melt caused by an increment of crystallization, dM_C . Similarly we solve for the change in concentration of a trace element in the solid, which, in the case where mass loss only occurs in the melt phase, evolves as:

$$\frac{dC_{C,b}}{dM_C} = \frac{DC_M - C_{C,b}}{M_C} \quad (5)$$

$C_{C,b}$ refers to the concentration in the bulk solid, rather than that which is instantaneously crystallized. Finally, the change in concentration in the lost melt phase is calculated as:

$$\frac{dC_L}{dM_C} = \frac{(C_M - C_L)}{M_L} \frac{dM_L}{dM_C} \quad (6)$$

where C_L is the concentration in the lost melt phase and M_L is the mass of melt lost. This model only accounts for melt loss; however, many SMB samples are enriched in incompatible trace elements, suggesting they may have accumulated melt (Fig. 4 and 5). When mass loss only occurs by removing mass from the solid, the change in concentration of a particular element in the solid instead evolves as:

$$\frac{dC_{C,b}}{dM_C} = \frac{DC_M}{M_C} - \frac{C_{C,b}}{M_C} \left[\frac{dM_{CL}}{dM_C} + 1 \right] \quad (7)$$

where M_{CL} is the mass of lost solid.

The group of ordinary differential equations above includes terms that account for the change in concentration associated with a small amount of crystallization (dM_C), as well as melt (dM_L) and crystal (dM_{CL}) loss. Here, melt loss is relevant to crystal accumulation whereas crystal loss is relevant to melt accumulation; however, the box model assumes no physical process by which these occur. The full derivation is included in the supplements. Crucially, the equations are derived with respect to M_C , which is the mass of crystallized solids. This means that if the functional forms of the mass of melt (M_L) and of lost crystals (M_{CL}) as function of mass crystallized are determined, then M_M can be solved for and the equations are completely resolved. We argue that in the limit that $D \gg 1$, the exact functional form of M_L and M_{CL} is of little importance (supplementary Fig. 1). The expressions for M_L and M_{CL} used in trace element calculations in this manuscript depend on M_L^F and M_{CL}^F , which are the final amount of melt or crystal loss as crystallization terminates. These parameters are solved for each SMB sample assuming a parental magma composition tabulated in Table 2.

Table 2. Composition of BC04 (assumed parental magma composition). Oxides are reported as wt % and elements as parts per million (ppm). Total Fe expressed as FeO.

SiO ₂	TiO ₂	Al ₂ O ₃	FeO	MnO	MgO	CaO	Na ₂ O	K ₂ O	P ₂ O ₅	Sr	Rb
73.60	0.30	13.74	1.64	0.05	0.44	1.67	3.74	4.73	0.08	203	144

Finally, knowledge of the bulk partition coefficient, D , is required in order to fully resolve the group of equations above. To accomplish this, we perform thermodynamic simulations using rhyolite-MELTS 1.1.x (Gualda & Ghiorso, 2015). Simulations assume a parental magma composition listed in Table 2, a fixed pressure of 200 MPa, ca. 5 wt % H₂O and an QFM+1 for the oxygen fugacity. The choice of parental magma composition is influenced by several observations. The pressure of 200 MPa is chosen due to the clustering of SMB samples along the 200 MPa minimum (Gualda *et al.*, 2012, Gualda *et al.*, 2023) of the Qz-Ab-Or ternary (supplementary Fig. 2), while the water content and oxygen fugacity are relatively unconstrained. However, the concentration of water must be sufficiently high to precipitate biotite as an early crystallizing phase (consistent with SMG mineralogy). The sensitivity of the results to these choices is explored by altering the wt % H₂O content to 2 wt % and the pressure to 500 MPa (supplementary Fig. 3 and 4). The starting temperature is set to assure the system is entirely comprised of melt and equilibrium crystallization proceeds in increments of 0.5°C until >95% of the mass is incorporated in the solid (usually ca. 730°C). Equilibrium crystallization is chosen because what is required for closure of the TE model is D as a function of mass crystallized. For trace element calculations, we model the evolution of both Sr and Rb using partition coefficients, K_D , reported in Table 3. The phase abundances predicted by rhyolite-MELTS as a function of crystallinity are shown in Fig. 11 as well as the associated evolution of the bulk partition coefficients for Sr and Rb. Example model outputs are included in Fig. 10.

Table 3. Table of partition coefficients used in trace element calculations.

	K_D^{Sr}	K_D^{Rb}
spinel	0 ^d	0 ^d
orthopyroxene	0.009 ^c	0.003 ^c
orthoclase	5.6 ^a	0.391 ^a
plagioclase	14 ^a	0.018 ^a
biotite	0.307 ^a	1.57 ^a
quartz	0 ^d	0 ^d
oxide	0 ^d	0 ^d

^a(Padilla & Gualda, 2016)

^bBachmann *et al.* (2005)

^cArth (1976)

^d Sr and Rb in quartz, oxides, and spinel are presumed to be perfectly incompatible (partition coefficients = 0).

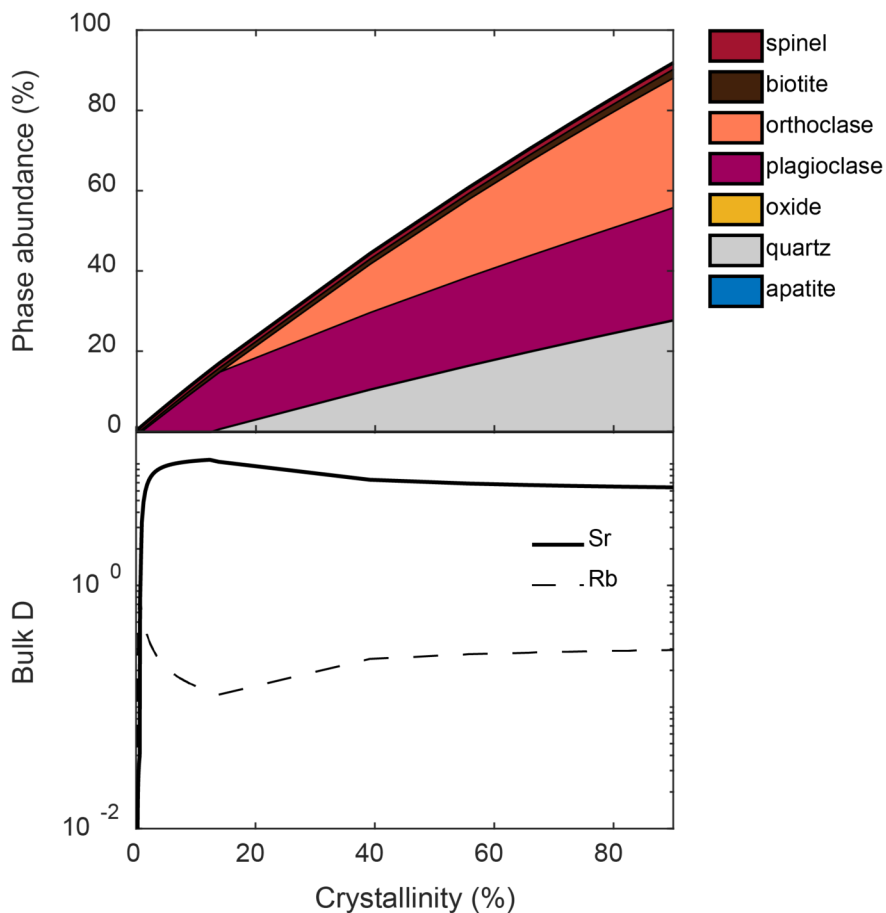


Figure 11: A) Phase abundances as predicted by rhyolite-MELTS 1.1.x (Gualda & Ghiorso, 2015). Phase abundance here is in terms of mass. B) Bulk partition coefficient, D , for Sr and Rb as a function of crystallinity. Simulations performed at 200 MPa, ca. 5 wt % H₂O, a starting composition listed in Table 2, and QFM+1 for the oxygen buffer. Note eutectic is reached at ca. 20 % crystallization.

The results of the thermodynamic simulations (phase mass as a function of temperature and composition of bulk liquid and bulk solids) are included in the supplementary Fig. 3, 4, and 5. In most cases, the majority of SMB data plot along tie-lines between solid and liquid equilibrium end members. When considering equilibrium crystallization, such as in these calculations, tie-lines connect liquid and solid lines of descent in equilibrium, while the exact points at which they are connected is a function of the mass crystallized (supplementary Fig. 5).

6. TRACE ELEMENT MODELING RESULTS – MELT AND CRYSTAL LOSS CALCULATIONS

Results from the trace element modeling suggest that the majority of samples from the upper portion of the SMB have accumulated significant amounts of Sr depleted melt. Samples from the lower portions of the batholith, on the other hand, show evidence of melt loss and crystal accumulation (Fig. 12). These results were obtained by solving for M_L^F in samples where the concentration of Sr is greater than that the assumed parental magma composition (Table 2) and by solving for M_{CL}^F in samples where the concentration of Sr is depleted compared to the assumed parental magma composition. The benefit of the trace element model is that it does not assume a physical process controlling phase separation.

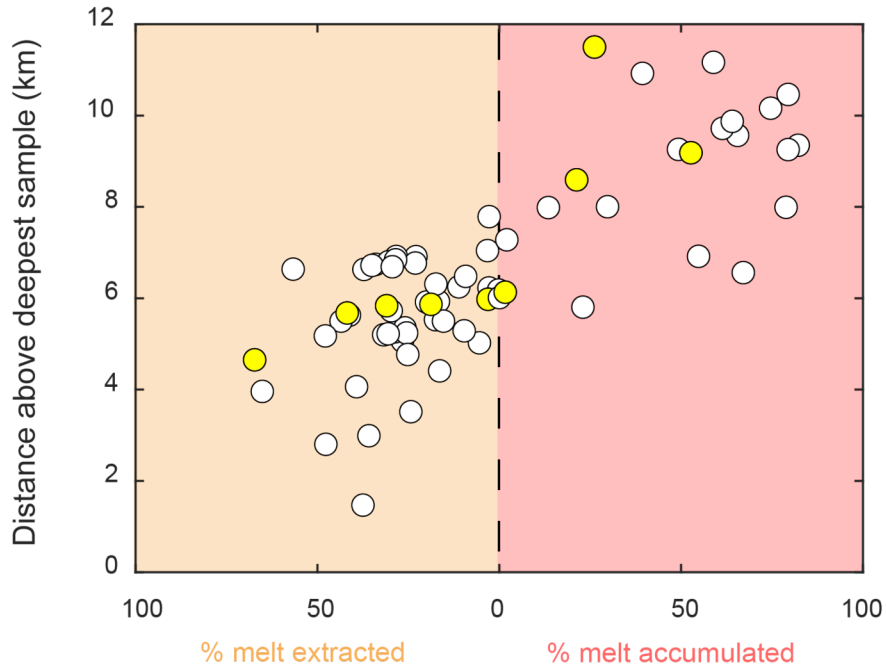


Figure 12: Distance above the deepest sample plotted as a function of mass loss calculated for each SMB sample. The vertical line indicating no melt loss corresponds to samples whose Sr concentrations are equivalent to that listed in Table 2 (assumed parental magma composition). The values on the left hand side of the x-axis were calculated by solving for total melt loss, M_L^F , while values on the right hand side of the x-axis were calculated by solving for total crystal loss, M_{CL}^F . Sample symbols here are identical to Fig. 4 and 5.

7. DISCUSSION

Conceptual model

The SMB is comprised of a patchwork of sills emplaced over ca. 2 Ma (Claiborne *et al.*, 2006, 2010, Miller *et al.*, 2011, Walker Jr *et al.*, 2007). Field relations, regional geology, and the plagioclase results presented in this study suggest that the sills that comprise the SMB crystallized from similar parental magma compositions. The conceptual model we invoke to explain the origins of Spirit Mountain batholith granites is mechanical phase separation by repacking-accommodated compaction (Bachmann & Huber, 2019, Boyer *et al.*, 2011, Holness *et al.*, 2017), a process likely repeated over periods of as much as several million years (emplacement of a sill like body of parental magma and subsequent crystallization and then compaction). Numerical models of compaction often consider the evolution of porosity or melt fraction of a continuous crystal column with an initially uniform melt fraction distribution (Bercovici *et al.*, 2001, Huber & Parmigiani, 2018, McKenzie, 1984, McKenzie, 1985, McKenzie, 2011, Ricard *et al.*, 2001). Melt and crystals separate due to their density contrast, which at melt fractions above the maximum packing

fraction (minimum melt fraction that can be obtained by particle reorganization) is likely accommodated by a combination of hindered settling and the rotation and translation of matrix crystals (repacking) (Bachmann & Huber, 2019, Boyer *et al.* , 2011, Holness *et al.* , 2017, Huber *et al.* , 2024). At any depth within the compacting layer, each sample can therefore be thought of as the sum of different proportions of melt and crystal components; proportions are controlled by melt-crystal separation, here driven by gravity. Under this idealized model, at depths nearest to the base within a single sill within the overall batholith, the driving force for phase separation is greatest and a layer depleted in trapped melt develops. At shallower depths the driving force for separation diminishes and less melt is lost. Meanwhile, at the top of the sill a melt rich layer develops. A consequence of this in the context of the SMB is the enrichment of CaO, Al₂O₃, Ba, and Sr, consistent with accumulation of feldspars in samples nearest to the base of the sills emplaced that comprise the pluton. Meanwhile, samples furthest from the base of a given sill within the pluton are SiO₂ rich and enriched in incompatible trace elements like Rb and Th, consistent with melt accumulation. Samples at intermediate depths, meanwhile, display chemical compositions intermediate to the two endmembers. Visually, this is manifested by intermediate samples plotting along mixing (or more precisely *unmixing*) tie-lines between melt and crystal endmembers located on either side of the parental composition (Payacán *et al.* , 2023). On the other hand, unmixing between melt and crystal compositions by phase separation occurring over a range of M_C, crystallized mass, (different points along equilibrium liquid and solid lines of descent) results in a wedge pattern on either side of the parental magma composition in major and trace element space and can explain the fact that not all samples collapse onto the same straight line (Fig. 4 and 5).

The melt and crystal loss calculations using Sr modeling predicts that the samples nearest to the base of the batholith, in general, have lost Sr-depleted melt (i.e. accumulated feldspar) to become enriched in Sr, while samples farthest from the base have lost crystals (i.e. accumulated evolved melt) (Fig. 12). Because the plagioclase crystals at all depths within a given sill have crystallized from the same magma, plagioclase composition in the cumulate crystals is for the most part invariant despite a broad range in major, minor, and trace element composition. The most melt, and therefore SiO₂, depleted samples, would be more albitic than would be expected if they had crystallized from a parental magma assumed to be compositionally equivalent to their bulk chemistry (Cornet *et al.* , 2022). Fig. 6 supports this interpretation for the SMB. Finally, melt loss is accompanied by detectable foliation in the most melt depleted samples nearest to the base of the pluton (Fig. 7 and 8).

Unmixing model - calculation of trapped melt fraction

While the TE model employed in earlier sections was used to calculate melt and crystal loss using only Sr, we make use of an alternate approach to calculate the trapped melt fraction and the range of crystallinities over which melt is lost. When plotting the Rb against Sr concentrations for the SMB (bulk) samples, the data collapses primarily onto a straight line defined by the samples belonging to the transect in Fig. 1b. We assume that the spread in Rb and Sr concentrations for the analyzed samples (yellow samples in prior figures and in Fig. 13) is due primarily to unmixing of fixed liquid and crystal end member compositions for reasons outlined in the previous section. The choice of parental magma composition is listed in Table 2 and is validated by field observations, the fact that the spread in major, minor, trace element with respect to wt % SiO₂ is minimized at compositions near the assumed parental magma composition, and the ability of the starting composition to satisfy the observed major, minor, and trace element data. The extent of crystallization (mass fraction) before melt loss can be solved for by calculating the evolution of Rb and Sr in the liquid and solid assuming fractional crystallization where melt and crystals aren't separated from one another and fitting the tie-lines between liquid and solid to the samples composition (Fig. 13). In this case, the crystallized mass fraction, M_C, that minimizes the scatter about the mixing line is 0.24. The trapped melt fraction of each sample is then calculated as the relative contribution of each endmember – the solid and liquid at M_C = 0.24 of a parental magma composition listed in Table 2. Using rhyolite-MELTS, we convert mass to volume and solve for the trapped melt volume (Fig. 13). The results are similar to the melt and crystal loss results, except this technique allows us to obtain the tie-line along which unmixing primarily occurs (i.e. how much mass has crystallized before the onset of unmixing). This allows us to quantify

trapped melt fraction profiles from the trace element record of the samples and compare to numerical models of (mechanical) compaction by repacking (Florez *et al.*, 2024).

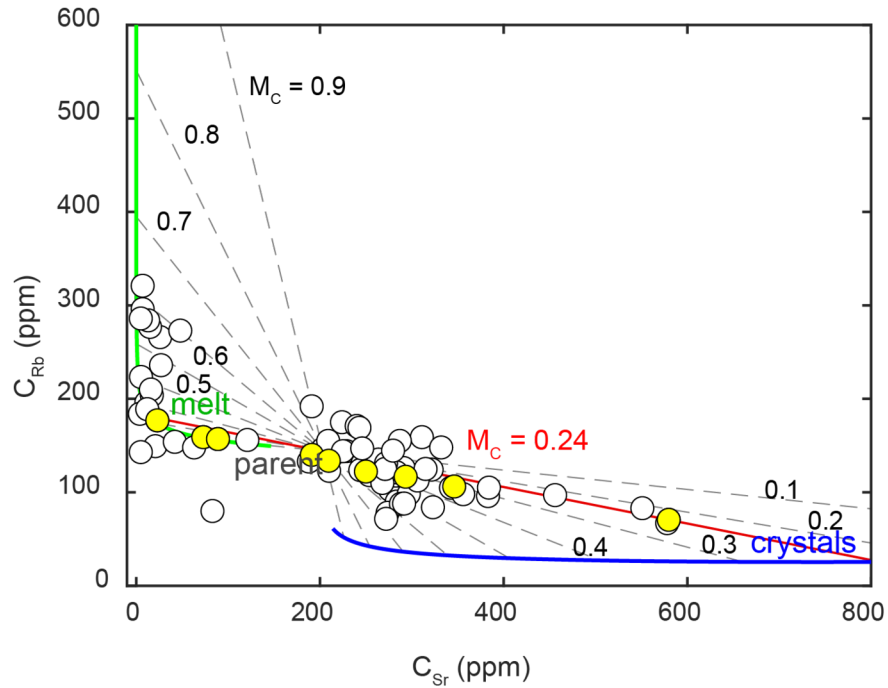


Figure 13: Trace element unmixing model compared to SMB samples. Tie lines relate the composition of liquid and solid in equilibrium with each other over a range of mass fraction crystallized M_C . These compositions are calculated assuming fractional crystallization of a parental magma where no melt loss occurs. The assumed parental magma composition is listed in Table 2. The prior sections suggest that the transect samples analyzed are mixtures of two chemically distinct reservoirs along unmixing or tie lines and justifies this choice. The tie line in red associated with $M_C = 0.24$ is the tie line that minimizes the least square error with respect to the analyzed samples in yellow.

Minimum trapped melt fraction and maximum packing fraction

An important result presented here is that the minimum trapped melt is ca. 30%. Lee and Morton (2015) analyzed plutons in the Peninsular Ranges Batholith and similarly relied on trace element compositions to estimate trapped melt fraction. They found similar results with 20-30% of residual melt trapped in cumulate at the root of high silica granites, arguing on that basis that hindered settling was likely responsible for melt-crystal separation. We propose that the lower limit of ca. 30% trapped melt is due to the transition in phase separation mechanisms from a hydrodynamic (melt-crystals interactions) and friction (crystal-crystal interactions) repacking dominated compaction regime to a compaction regime dominated by viscous creep such as grain-boundary diffusion-controlled creep. Repacking is efficient at intermediate melt fractions, as individual grains do not need to be deformed to accommodate pore closure (Boyer *et al.*, 2011). However, as the maximum packing fraction is approached, this is no longer the case and the resistance to pore space closure associated with repacking diverges (Boyer *et al.*, 2011). At melt fractions lower than the maximum packing fraction, pore space can only be closed by deformation of grains. Pore closure at melt fractions lower than the maximum packing fraction is much less efficient than pore space closure by repacking at intermediate melt fractions. This common minimum trapped melt fraction inferred for SMB and the Peninsular Ranges Batholith suggests that once compaction by repacking reaches the maximum packing fraction (around 0.3 trapped melt), further compaction involves processes that are too slow to be active before the thermal death

of these plutons.

Driving force for melt extraction at SMB

The increase of intensity of fabric with depth in planes illustrated in Fig. 7, manifested as an increase in alignment factor, AF, with depth (Fig. 7 and 8), suggests that the process controlling melt loss is grain reorganization (repacking). The correlation between AF and paleodepth in transect samples analyzed by the unmixing models provides evidence that gravity is the driving force behind melt extraction. Under such conditions, we perform a series of simple calculations to determine the time required to develop a melt rich horizon of a given thickness atop a compacting crystal matrix (Fig. 14). The melt rich horizon is formed by the extraction and accumulation of interstitial melt in the crystal matrix. The interstitial melt at the top of the crystal mush is constant as there is no driver for melt extraction matrix (the pressure in crystal matrix and melt at the top are equal). Instead, melt is extracted from below and migrates upwards, lowering the height of the crystal matrix and developing a melt rich layer. To solve for F_{TL} as a function of height in a compacting layer of crystals with interstitial melt, we consider a combined statement of momentum conservation between crystal matrix and melt (Florez *et al.*, 2024),

$$(1 - F_{TL}) \rho g = -\beta F_{TL} (V_m - V_s) - \left(\frac{\partial}{\partial z} \left[(1 - F_{TL}) \left(\frac{\gamma}{F_{TL}} + 1 \right) \xi \frac{\partial}{\partial z} V_s \right] \right) \quad (8a)$$

and statement of mass conservation,

$$\frac{\partial F_{TL}}{\partial t} + \frac{\partial}{\partial z} [F_{TL} V_m] = 0 \quad (8b)$$

Here, β is proportional to $\frac{\mu_m}{K}$, where μ_m is the melt viscosity and K is the permeability of the crystal matrix, V_s and V_m are the crystal matrix and melt velocity, respectively, ρ is the density difference between crystal and melt, g is the gravitational constant, z is depth within the compacting layer, γ is a geometric constant, and ξ is the viscous resistance to pore space closure in the crystal matrix (effective matrix viscosity). Critically, ξ is a function of F_{TL} that depends on the mechanism by which pore space in the matrix is closed. Eq. (8a) is in essence a force balance where $-\beta F_{TL} (V_m - V_s)$ is a drag force, $(1 - F_{TL}) \rho g$ is a buoyancy force, and $\left(\frac{\partial}{\partial z} \left[\left(\frac{\gamma}{F_{TL}} + 1 \right) (1 - F_{TL}) \xi \frac{\partial}{\partial z} (F_{TL} [V_m - V_s]) \right] \right)$ is a compaction force. Here, melt and crystal matrix flow is driven by the buoyancy force.

The compaction model solves for the mass and momentum conservation of the two phases (melt and crystals) which provides us with the evolution of F_{TL} and mechanical phase velocities (velocity of melt and crystal) in a compacting crystal column as a function of time. Mass conservation is solved with an upwind and the momentum conservation with a centered finite volume scheme. The results of these simulations are strongly influenced by the effective matrix viscosity, ξ . Here, we use an expression for ξ assuming that pore closure in the matrix is accommodated by repacking (particle rearrangements in the absence of deformation of individual grains):

$$\xi = \xi_0 \left(\frac{4}{3} \left[1 + \frac{5}{2} (1 - F_{TL}) \left(1 - \frac{1 - F_{TL}}{1 - F_{TL}^m} \right)^{-1} + 0.3 \left(\frac{1 - F_{TL}}{F_{TL} - F_{TL}^m} \right)^2 \right] + \left[\frac{1 - F_{TL}}{F_{TL} - F_{TL}^m} \right]^2 \right) \quad (9)$$

In this regime, ξ depends on F_{TL}^m , which is the lowest F_{TL} of an aggregate that can be obtained by particle rearrangements, and a reference viscosity, ξ_0 . Using $F_{TL}^m = 0.3$ and $\xi_0 = 10^6$ Pa s can explain the SMB trapped melt profiles reasonably well in that the lowest F_{TL} value calculated using the unmixing model is 0.32 (Fig. 14). The F_{TL}^m and ξ_0 predicted in Florez *et al.* (2024) by employing the numerical compaction model to high temperature and pressure mechanical phase separation experiments were ca. 0.3 and $10^5 - 10^6$ Pa s, respectively. Under such conditions, we expect that the timescales for melt extraction and formation of the approximately 3.5 km thick region of pure melt above the transect to be ca. 30 ka for melt with viscosity of 10^5 Pa s and a grain diameter of 5 mm (Fig. 14).

The model is described in further detail in Florez *et al.* (2024). Because of the longevity of the SMB, it is not surprising then that significant melt loss has occurred throughout the majority of the SMG samples.

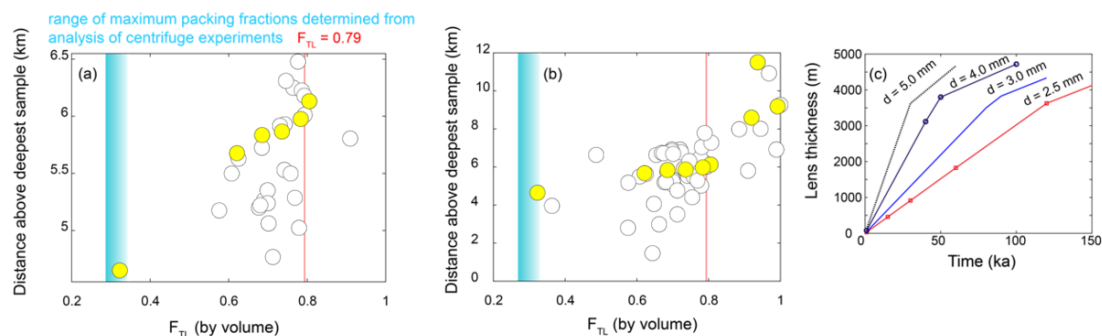


Figure 14: A) Volumetric trapped melt fraction (F_{TL}) for each SMG sample analyzed in transect (yellow) and all (white) SMG samples calculated using the trace element unmixing model. Trapped melt calculations are made by projecting sample data orthogonally onto the $M_C = 0.24$ tie line and using the lever rule to determine relative proportions of both melt and cumulate end members. Range of maximum packing fractions (in terms of melt fraction) determined from analysis of centrifuge experiments in Florez *et al.* (2024) are superimposed. Here, a value of ca. 0.3 aligns well with the minimum observed melt fraction estimates. B) F_{TL} over entire exposed batholith. C) Forward simulations to calculate the time required to form an eruptible melt horizon of a given thickness using the forward model from Florez *et al.* (2024). Here, the calculations are performed using different grain diameters.

8. CONCLUSIONS

This work adds to the growing catalogue of research describing the cumulate origins of intermediate and silicic plutons and geochemical and textural evidence of phase separation in these systems (Bachl *et al.*, 2001, Barnes *et al.*, 2019, Claiborne *et al.*, 2006, Claiborne *et al.*, 2010, Cornet *et al.*, 2022, Fiedrich *et al.*, 2017, Garibaldi *et al.*, 2018, Gelman *et al.*, 2014, Hartung *et al.*, 2017, Payacán *et al.*, 2023, Schaeen *et al.*, 2018, Tavazzani *et al.*, 2020, Walker Jr *et al.*, 2007). The textures and chemistry of the samples suggest that the range in chemical compositions recorded by SMB samples is consistent with phase separation by repacking-accommodated compaction. Trace element modeling suggests that 24% of the mass has crystallized magma of uniform composition before unmixing occurs, explaining the composition of the majority of SMB. We find in the cumulates that the trapped melt fraction is correlated with wt % SiO_2 and incompatible trace elements and inversely correlated with depth, fabric intensity, and compatible trace elements. We argue that the batholith is the result of partial-crystallization and subsequent mechanical phase separation by repacking-driven compaction of repeated injections of similar magmas over the course of about two million years as indicated by zircon age dates by previous researchers (Claiborne *et al.*, 2006, 2010, Walker Jr *et al.*, 2007).

ACKNOWLEDGEMENTS

We appreciate the help of Julien Allaz and Alejandro Cortes Calderon in the acquisition of EPMA data at the ETH electron microscopy lab. This work was supported by the National Science Foundation grant EAR-2021328.

DATA AVAILABILITY STATEMENT

Code and scripts used for numerical model are available at <https://doi.org/10.24433/CO.9041342.v1>. Geochemical datasets presented are available at <https://doi.org/10.60520/IEDA/113194>.

REFERENCES

- Bachl, C. A., Miller, C. F., Miller, J. S. & Faulds, J. E. (2001). Construction of a pluton: Evidence from an exposed cross section of the Searchlight pluton, Eldorado Mountains, Nevada. *Geological Society of America Bulletin* **113** , 1213-1228.
- Bachmann, O. & Huber, C. (2019). The inner workings of crustal distillation columns; the physical mechanisms and rates controlling phase separation in silicic magma reservoirs. *Journal of Petrology* **60** , 3-18.
- Bachmann, O., Miller, C. F. & De Silva, S. (2007). The volcanic–plutonic connection as a stage for understanding crustal magmatism. *Journal of Volcanology and Geothermal Research* **167** , 1-23.
- Barnes, C. G., Werts, K., Memeti, V. & Ardill, K. (2019). Most granitoid rocks are cumulates: deductions from hornblende compositions and zircon saturation. *Journal of Petrology* **60** , 2227-2240.
- Barraud, J. (2006). The use of watershed segmentation and GIS software for textural analysis of thin sections. *Journal of Volcanology and Geothermal Research* **154** , 17-33.
- Bercovici, D., Ricard, Y. & Schubert, G. (2001). A two-phase model for compaction and damage: 1. General theory. *Journal of Geophysical Research: Solid Earth* **106** , 8887-8906.
- Boyer, F., Guazzelli, E. & Pouliquen, O. (2011). Unifying suspension and granular rheology. *Physical review letters* **107** , 188301.
- Claiborne, L. L., Miller, C., Walker, B., Wooden, J., Mazdab, F. & Bea, F. (2006). Tracking magmatic processes through Zr/Hf ratios in rocks and Hf and Ti zoning in zircons: an example from the Spirit Mountain batholith, Nevada. *Mineralogical Magazine* **70** , 517-543.
- Claiborne, L. L., Miller, C. F. & Wooden, J. L. (2010). Trace element composition of igneous zircon: a thermal and compositional record of the accumulation and evolution of a large silicic batholith, Spirit Mountain, Nevada. *Contributions to Mineralogy and Petrology* **160** , 511-531.
- Coleman, D. S., Gray, W. & Glazner, A. F. (2004). Rethinking the emplacement and evolution of zoned plutons: Geochronologic evidence for incremental assembly of the Tuolumne Intrusive Suite, California. *Geology* **32** , 433-436.
- Cornet, J., Bachmann, O., Ganne, J., Fiedrich, A., Huber, C., Deering, C. D. & Feng, X. (2022). Assessing the effect of melt extraction from mushy reservoirs on compositions of granitoids: From a global database to a single batholith. *Geosphere* **18** , 985-999.
- Deering, C. & Bachmann, O. (2010). Trace element indicators of crystal accumulation in silicic igneous rocks. *Earth and Planetary Science Letters* **297** , 324-331.
- Drake, M. J. (1976). Plagioclase—melt equilibria. *Geochimica et Cosmochimica Acta* **40** , 457-465.
- Dungan, M. A., Long, P. E. & Rhodes, J. (1978). Magma mixing at mid-ocean ridges: Evidence from legs 45 and 46-DSDP. *Geophysical Research Letters* **5** , 423-425.
- Faulds, J. E., Feuerbach, D. L., Miller, C. F. & Smith, E. I. (2001). Cenozoic evolution of the northern Colorado River extensional corridor, southern Nevada and northwest Arizona.
- Faulds, J. E., Feuerbach, D. L., Reagan, M. K., Metcalf, R. V., Gans, P. & Walker, J. D. (1995). The Mount Perkins block, northwestern Arizona: An exposed cross section of an evolving, preextensional to synextensional magmatic system. *Journal of Geophysical Research: Solid Earth* **100** , 15249-15266.
- Faulds, J. E., Geissman, J. W. & Mawer, C. K. (1990). Structural development of a major extensional accommodation zone in the Basin and Range Province, northwestern Arizona and southern Nevada; Implications for kinematic models of continental extension. *Basin and range extensional tectonics near the latitude of Las Vegas, Nevada: Geological Society of America Memoir* **176** , 37-76.

- Faulds, J. E., Geissman, J. W. & Shafiqullah, M. (1992). Implications of paleomagnetic data on Miocene extension near a major accommodation zone in the Basin and Range province, northwestern Arizona and southern Nevada. *Tectonics* **11** , 204-227.
- Fiedrich, A. M., Bachmann, O., Ulmer, P., Deering, C. D., Kunze, K. & Leuthold, J. (2017). Mineralogical, geochemical, and textural indicators of crystal accumulation in the Adamello Batholith (Northern Italy). *American Mineralogist* **102** , 2467-2483.
- Florez, D., Huber, C., Hoyos, S., Pec, M., Parmentier, E. M., Connolly, J. A. D. & Hirth, G. (2024). Repacking in Compacting Mushes at Intermediate Melt Fractions: Constraints from Numerical Modeling and Phase Separation Experiments on Granular Media. *Authorea Preprints* .
- Garibaldi, N., Tikoff, B., Schaen, A. J. & Singer, B. S. (2018). Interpreting granitic fabrics in terms of rhyolitic melt segregation, accumulation, and escape via tectonic filter pressing in the Huemul pluton, Chile. *Journal of Geophysical Research: Solid Earth* **123** , 8548-8567.
- Gelman, S. E., Deering, C. D., Bachmann, O., Huber, C. & Gutierrez, F. J. (2014). Identifying the crystal graveyards remaining after large silicic eruptions. *Earth and Planetary Science Letters* **403** , 299-306.
- Glazner, A. F., Bartley, J. M., Coleman, D. S., Gray, W. & Taylor, R. Z. (2004). Are plutons assembled over millions of years by amalgamation from small magma chambers? *GSA today* **14** , 4-11.
- Gualda, G. A. & Ghiorso, M. S. (2015). MELTS - Excel: A Microsoft Excel-based MELTS interface for research and teaching of magma properties and evolution. *Geochemistry, Geophysics, Geosystems* **16** , 315-324.
- Gualda, G. A., Ghiorso, M. S., Lemons, R. V. & Carley, T. L. (2012). Rhyolite-MELTS: a modified calibration of MELTS optimized for silica-rich, fluid-bearing magmatic systems. *Journal of Petrology* **53** , 875-890.
- Gualda, G. A. R., Miller, C. F. & Wallrich, B. M. (2023). The Rhyolite Factory: Insights from rhyolite-MELTS geobarometry of plutonic rocks and associated volcanics.
- Haapala, I., Ramo, O. T. & Frindt, S. (2005). Comparison of Proterozoic and Phanerozoic rift-related basaltic-granitic magmatism. *Lithos* **80** , 1-32.
- Hartung, E., Caricchi, L., Floess, D., Wallis, S., Harayama, S., Kouzmanov, K. & Chiaradia, M. (2017). Evidence for residual melt extraction in the Takidani Pluton, Central Japan. *Journal of Petrology* **58** , 763-788.
- Holness, M. B., Vukmanovic, Z. & Mariani, E. (2017). Assessing the role of compaction in the formation of adcumulates: a microstructural perspective. *Journal of Petrology* **58** , 643-673.
- Howard, K., Wooden, J., Simpson, R. & Pease, V. (1996). Extension-related plutonism along the Colorado River extensional corridor. *Geological Society of America Abstracts with Programs* , 251.
- Howard, K. A. & John, B. E. (1987). Crustal extension along a rooted system of imbricate low-angle faults: Colorado River extensional corridor, California and Arizona. *Geological Society, London, Special Publications* **28** , 299-311.
- Howard, K. A., John, B. E., Davis, G., Anderson, J. & Gans, P. (1994). A guide to Miocene extension and magmatism in the lower Colorado River region, Nevada, Arizona, and California. US Geological Survey.
- Huber, C., Parmentier, E. M. & Florez, D. (2024). Particle sedimentation in a fluid at low Reynolds number: a generalization of hindered settling described by a two-phase continuum model. *AGU23* .
- Huber, C. & Parmigiani, A. (2018). A physical model for three-phase compaction in silicic magma reservoirs. *Journal of Geophysical Research: Solid Earth* **123** , 2685-2705.
- Lee, C.-T. A. & Morton, D. M. (2015). High silica granites: Terminal porosity and crystal settling in shallow magma chambers. *Earth and Planetary Science Letters* **409** , 23-31.

- McKenzie, D. (1984). The generation and compaction of partially molten rock. *Journal of Petrology* **25** , 713-765.
- McKenzie, D. (1985). The extraction of magma from the crust and mantle. *Earth and Planetary Science Letters* **74** , 81-91.
- McKenzie, D. (2011). Compaction and crystallization in magma chambers: towards a model of the Skaergaard intrusion. *Journal of Petrology* **52** , 905-930.
- Miller, C. F., Furbish, D. J., Walker, B. A., Claiborne, L. L., Koteas, G. C., Bleick, H. A. & Miller, J. S. (2011). Growth of plutons by incremental emplacement of sheets in crystal-rich host: Evidence from Miocene intrusions of the Colorado River region, Nevada, USA. *Tectonophysics* **500** , 65-77.
- Payacan, I., Gutierrez, F., Bachmann, O. & Parada, M. A. (2023). Differentiation of an upper crustal magma reservoir via crystal-melt separation recorded in the San Gabriel pluton, central Chile. *Geosphere* **19** , 348-369.
- Putirka, K. D. (2008). Thermometers and barometers for volcanic systems. *Reviews in Mineralogy and Geochemistry* **69** , 61-120.
- Rhodes, J., Dungan, M., Blanchard, D. & Long, P. (1979). Magma mixing at mid-ocean ridges: evidence from basalts drilled near 22 N on the Mid-Atlantic Ridge. *Tectonophysics* **55** , 35-61.
- Ricard, Y., Bercovici, D. & Schubert, G. (2001). A two-phase model for compaction and damage: 2. Applications to compaction, deformation, and the role of interfacial surface tension. *Journal of Geophysical Research: Solid Earth* **106** , 8907-8924.
- Schaen, A. J., Singer, B. S., Cottle, J. M., Garibaldi, N., Schoene, B., Satkoski, A. M. & Fournelle, J. (2018). Textural and mineralogical record of low-pressure melt extraction and silicic cumulate formation in the late Miocene Risco Bayo–Huemul plutonic complex, southern Andes. *Journal of Petrology* **59** , 1991-2016.
- Tavazzani, L., Peres, S., Sinigoi, S., Demarchi, G., Economos, R. & Quick, J. (2020). Timescales and mechanisms of crystal-mush rejuvenation and melt extraction recorded in Permian plutonic and volcanic rocks of the Sesia Magmatic System (southern Alps, Italy). *Journal of Petrology* **61** , ega049.
- Walker Jr, B. A., Miller, C., Claiborne, L. L., Wooden, J. & Miller, J. (2007). Geology and geochronology of the Spirit Mountain batholith, southern Nevada: Implications for timescales and physical processes of batholith construction. *Journal of Volcanology and Geothermal Research* **167** , 239-262.